

Directional illumination analysis using the local exponential frame

Jian Mao¹, Ru-Shan Wu³, and Jing-Huai Gao²

ABSTRACT

We have developed an efficient method of directional illumination analysis in the local angle domain using local exponential frame beamlets. The space-domain wavefields with different shot-receiver geometries are decomposed into the local angle domain by using the local exponential beamlets, which form a tight frame with the redundancy ratio two and are implemented by a linear combination of local cosine and local sine transforms. Because of the fast algorithms of the local cosine/sine transforms, this method is much more efficient than the previously used decomposition methods in directional illumination analysis, such as the local slant-stacking method and the Gabor-Daubechies frame method. The results of directional illumination (DI) maps and the acquisition dip responses (ADR) for the 2D SEG/EAGE salt model and the 45-shot 3D SEG/EAGE model demonstrated the validity and feasibility of our method. Compared with the illumination results using local slant-stacking decomposition, the new method produces illumination maps of similar quality, but it does so a few times faster. Furthermore, because of its high computational efficiency and saving in memory usage, the new method makes the 3D directional illumination analysis readily applicable in the industry.

INTRODUCTION

Directional illumination analysis in a target area is a powerful tool to study the influence of acquisition configuration and overlying structure on the quality of a migration image (e.g., [Chen et al., 2006](#); [Xie et al., 2006](#)). Many techniques of predicting illumination intensity distributions for certain acquisition geometries are based on ray-tracing modeling ([Berkhout, 1997](#); [Schneider and Winbow, 1999](#);

[Bear et al., 2000](#); [Muerdter and Ratcliff, 2001a, 2001b](#); [Muerdter et al., 2001](#)). Recently, the applicability of the ray-tracing method has been improved (e.g., [Gjøystdal et al., 2007](#)). Although ray tracing is convenient and efficient, it still has some limitations, e.g., the resultant illumination maps might contain large errors in complex areas because of the high-frequency approximation and the singularity problems of ray theory ([Hoffmann, 2001](#)). Therefore, wave-theory-based methods are much more desirable to obtain reliable and frequency-dependent illuminations.

One-way wave-equation-based propagators are widely used in illumination analysis ([Xie et al., 2006](#); [Etgen, 2008](#)). They can handle multiforward-scattering phenomena, including focusing/defocusing, and diffraction. However, unlike the ray-based methods, the wavefield obtained from traditional wave-equation-based methods, such as finite-difference-based one-way propagators ([Claerbout, 1985](#)), the Fourier finite-difference method ([Ristow and Rühl, 1994](#)), and the generalized screen propagator ([Xie and Wu, 1998](#); [Le Rousseau and de Hoop, 2001](#)), do not explicitly give the directional information in the propagation process. Techniques to obtain the local angle-domain information of a space-domain wavefield based on the beamlet decomposition or local slant stacking have been developed and applied to directional illumination analysis ([Xie and Wu, 2002](#); [Wu et al., 2003](#); [Luo et al., 2004](#); [Wu and Chen, 2002, 2003, 2006](#); [Xie et al., 2003, 2006](#)).

Full-wave (two-way)-equation-based illumination analysis provides full-angle true-amplitude illuminations of all arrivals for the survey design. The full-wave modeling and the local angle-domain illumination analysis can be implemented in the time domain or in the frequency domain. [Xie and Yang \(2008\)](#) propose an illumination method that uses a time-domain full-wave finite-difference propagator and a time-domain local slowness analysis to determine the angle information. The method is effective in the illumination analysis for reverse-time migration. [Cao and Wu \(2009\)](#) propose a frequency-domain full-wave directional illumination analysis method, which can be used for frequency-dependent illumination analysis. The

Manuscript received by the Editor 22 April 2009; revised manuscript received 31 January 2010; published online 22 September 2010; corrected version published online 27 September 2010.

¹University of California at Santa Cruz, Department of Earth and Planetary Sciences, Modeling and Imaging Laboratory, Santa Cruz, California, U.S.A., and Xi'an Jiaotong University, Department of Electronic and Information Engineering, Institute of Wave and Information, Xi'an, China. E-mail: arrowspirit@gmail.com.

²Xi'an Jiaotong University, Department of Electronic and Information Engineering, Institute of Wave and Information, Xi'an, China. E-mail: jhgao@mail.xjtu.edu.cn.

³University of California at Santa Cruz, Department of Earth and Planetary Sciences, Modeling and Imaging Laboratory, Santa Cruz, California, U.S.A. E-mail: wrs@es.ucsc.edu.

© 2010 Society of Exploration Geophysicists. All rights reserved.

computational cost is still a problem for full-wave methods. In many cases, one-way methods are still very useful with good accuracy, better efficiency, and fewer artifacts.

Illumination analysis also provides useful information for the compensation of the image amplitude. [Rickett \(2003\)](#) proposes an illumination-based normalization for wave-equation depth migration. However, the illumination calculated in that paper is the total illumination and lacks directional information. As a consequence, it cannot give a good compensation to the image amplitude in the area where the structures are angle dependent. For the amplitude compensation, directional illumination is needed for a limited acquisition aperture and is critical in balancing the image amplitude, especially for weak interfaces in poorly illuminated regions. Illumination-based true-amplitude, true-reflection migration methods also have been studied extensively ([Wu et al., 2004](#); [Audebert et al., 2005](#); [Cao and Wu, 2005, 2008](#); [Lecomte 2008](#)).

With new advancements in seismic acquisition for 3D surveys, some illumination studies have been carried out for 3D cases (e.g., [Fontecha et al., 2005](#); [Alai and Thorbecke, 2008](#); [Droujinine et al., 2008](#)) and for a 3D vertical seismic profiling (VSP) data set (e.g., [Yu et al., 2005](#)). However, the present methods, such as the local plane-wave decomposition, have poor efficiency for 3D data sets. The non-orthogonal Gabor-Daubechies frame decomposition needs at least a redundancy ratio of four in the wavefield representation ([Chen et al., 2006](#)), which results in huge computational cost. The local slant stacking for wavefield decomposition is even more computationally demanding.

The local cosine bases (LCB) decomposition applied to the seismic wavefield ([Wang and Wu, 2002](#); [Wu et al., 2000, 2008](#); [Wang et al., 2003](#); [Wu and Mao, 2007](#)) is efficient in wavefield decomposition, and the corresponding propagator was successfully developed for wave propagation and imaging. Because the local cosine transform is orthogonal and has a fast algorithm, the wavefield decomposition and extrapolation using the LCB beamlet have good computational efficiency. Nevertheless, local cosine beamlets always propagate along two symmetrical directions with respect to the vertical axis. This lack of uniquely defined directional localization prevents its use for directional illumination analysis. Therefore, we need a more efficient way to do directional illumination analysis in the 3D case.

In this work, we propose a decomposition method using local exponential frame beamlets. The local exponential frame is a tight frame with the redundancy ratio two, which is formed by linear combinations of local cosine and local sine bases. The tests presented in

this paper are based on the one-way wave-equation, but this new beamlet decomposition method can be extended to the full-wave illumination in the frequency domain. This newly developed local exponential frame beamlet has uniquely defined directional localization. By taking advantage of the fast algorithm of local cosine/sine transforms, this method can provide local angle-domain information efficiently. We apply the method to the illumination analysis of the 2D SEG/EAGE model and compare it with the local slant-stacking method. We also extend this method to the 3D case, and calculate illumination distribution on a 3D SEG/EAGE salt model.

LOCAL TRIGONOMETRIC BASES AND LOCAL EXPONENTIAL FRAMES

The frequency-space-domain wavefield can be decomposed into beamlets, which provides us the localized information in both space and direction simultaneously. Beamlet transform uses a translated window for the spatial localization and harmonic modulations for the directional localization. Both orthogonal bases (e.g., local cosine bases) ([Wu et al., 2008](#)) and tight frames (e.g., Gabor-Daubechies frame) ([Chen et al., 2006](#); [Wu and Chen, 2006](#)) were introduced into the beamlet decomposition.

For the consideration of computational efficiency, we prefer orthogonal bases, which have no redundancy and have efficient decomposition and reconstruction. However, the Balian-Low theorem ([Balian, 1981](#); [Daubechies, 1992](#)) states that orthogonal bases generated by Gaussian windowed exponential functions, with localization in both space and wavenumber, do not exist. Redundancy is needed to have a stable reconstruction. On the other hand, [Coifman and Meyer \(1991\)](#) (see also [Wickerhauser, 1994](#); [Mallat, 1999](#)) successfully constructed local trigonometric bases (LTB), including local cosine/sine bases (LCB/LSB), which have an almost ideal localization in the space and wavenumber domains. The only exception is that the localization in the wavenumber domain is in the form of two symmetrical (LCB) or antisymmetrical (LSB) lobes. This two-lobe localization is the price paid for the orthogonality of the decomposition bases.

Local trigonometric bases

Local trigonometric bases consist of the cosine/sine multiplied by smooth, compactly supported bell functions. In fact, these orthonormal bases are formed by linear combinations from a tight frame of local exponentials ([Daubechies et al., 1991](#); [Auscher, 1994](#)). A local cosine/sine basis element can be specified by its spatial position \bar{x}_n , interval (the nominal length of the window) $L_n = \bar{x}_{n+1} - \bar{x}_n$, and the wavenumber index m ($m = 0, \dots, M-1$, M denotes the sample point number of each interval; $n = 0, \dots, N-1$, N denotes the total interval number) as follows:

$$b_{mn}^{(c)}(x) = \sqrt{\frac{2}{L_n}} B_n(x) \cos\left(\pi\left(m + \frac{1}{2}\right) \frac{x - \bar{x}_n}{L_n}\right) \quad (1)$$

and

$$b_{mn}^{(s)}(x) = \sqrt{\frac{2}{L_n}} B_n(x) \sin\left(\pi\left(m + \frac{1}{2}\right) \frac{x - \bar{x}_n}{L_n}\right), \quad (2)$$

where $b_{mn}^{(c)}(x)$ and $b_{mn}^{(s)}(x)$ denote the local cosine and local sine bases, respectively (Figure 1). The expression $B_n(x)$ denotes a bell function, which is smooth and supported in the compact interval $[\bar{x}_n$

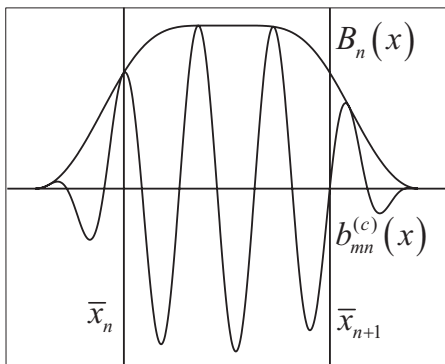


Figure 1. An element of local cosine bases.

$-\varepsilon, \bar{x}_{n+1} + \varepsilon']$ for $\bar{x}_n + \varepsilon \leq \bar{x}_{n+1} - \varepsilon'$, with $\varepsilon, \varepsilon'$ as the left and right overlapping radius, respectively. Appendix A gives the definition of the bell function in detail.

As the local trigonometric bases are modulated harmonic functions, they are suitable for wavefield decomposition. Combined with its orthogonal character, the LTB ensures the sparseness of the decomposition coefficients, which results in effective and efficient wavefield representation. Wu et al. (2008) constructed a local cosine basis beamlet propagator, which has proved to be an accurate and efficient one-way propagator. Although the LCB gives us high-quality migration images, it lacks the capability to provide the complete directional information due to the ‘‘two-lobe’’ localization property.

If the LTB is used for the space-domain wavefield decomposition, $\pi(m + \frac{1}{2})/L_n$ can be related to the local horizontal wavenumber, which is related to propagating angles (the relationship between the local wavenumber and local angle will be discussed later). With $\bar{\xi}_m = \pi(m + \frac{1}{2})/L_n$ defined as the local horizontal wavenumber, the expression of the LCB can be rewritten as the following:

$$b_{mn}^{(c)}(x) = \frac{1}{2} \sqrt{\frac{2}{L_n}} B_n(x) [\exp(i\bar{\xi}_m(x - \bar{x}_n)) + \exp(-i\bar{\xi}_m(x - \bar{x}_n))]. \quad (3)$$

The two exponential terms indicate that an LCB beamlet always has two symmetrical propagating directions. Figure 2 shows the propagation of a single LCB beamlet in the 2D SEG/EAGE salt model. As a result, the LCB or LSB cannot be directly used in directional illumination analysis due to this lack of uniquely defined directional localization. Therefore, we need to go back to the tight frame representation with local exponentials for complete directional information.

Local exponential frame

The local exponential frame (LEF) atoms can be defined as

$$g_{mn}(x) = \sqrt{\frac{2}{L_n}} B_n(x) \exp(i\bar{\xi}_m(x - \bar{x}_n)), \quad (4)$$

where $m = -M, \dots, -1, 0, \dots, M-1$ and $n = 0, \dots, N-1$; M and N have the same definition for the LTB. To take advantage of the fast algorithm for the LCB/LSB transform, we separate the local exponential functions into two sets as follows:

$$\begin{cases} g_{mn}^{(+)}(x) = b_{mn}^{(c)}(x) + ib_{mn}^{(s)}(x) = \sqrt{\frac{2}{L_n}} B_n(x) \exp(i\bar{\xi}_m(x - \bar{x}_n)) \\ g_{mn}^{(-)}(x) = b_{mn}^{(c)}(x) - ib_{mn}^{(s)}(x) = \sqrt{\frac{2}{L_n}} B_n(x) \exp(-i\bar{\xi}_m(x - \bar{x}_n)) \end{cases}, \quad (5)$$

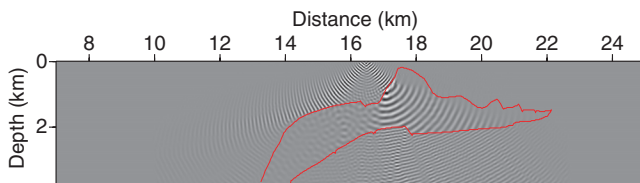


Figure 2. Local cosine beamlet propagation in the 2D SEG/EAGE salt model.

where $m = 0, \dots, M-1$. We will call $g_{mn}^{(+)}(x)$ and $g_{mn}^{(-)}(x)$ the right- and left-propagating local exponential beamlets, respectively. The LEF expressions indicate that they are linear combinations of the LCB and LSB.

For a real-value series, the number of LCB decomposition coefficients is the same as the total sample number of the original series because of the orthogonal characteristic. However, the number of the LEF decomposition coefficients is twice as many as the total sample number, which makes the LEF a frame of the redundancy ratio two. The dual-frame function for reconstruction is completely the same as the frame used for decomposition, which means the LEF is a tight frame. Collectively, $g_{mn}^{(+)}(x)$ and $g_{mn}^{(-)}(x)$ form a tight frame of the redundancy ratio two (Daubechies et al., 1991; Auscher, 1994). Compared with the Gabor-Daubechies frame, the local exponential frame does not need a dual-frame calculation and can be implemented efficiently by using the fast algorithm of the LTB.

The other important characteristic of the LEF that concerns us is the frequency leakage (see Appendix A for a discussion). Figure 3 shows how the LEF beamlet propagates in the 2D SEG/EAGE salt model, which gives the localized information with the uniquely defined direction. The leakage of the LEF beamlets to other directions (wavenumbers) is barely seen. As a result of this directional character, the LEF is more suitable than the LCB for wave representation with sparse decomposition coefficients.

WAVEFIELD DECOMPOSITION IN THE LOCAL WAVENUMBER DOMAIN USING THE LOCAL EXPONENTIAL FRAME BEAMLET

Generally, in the frequency-space (f - x) domain, the scalar wave equation can be written as

$$[\partial_x^2 + \partial_z^2 + \omega^2/V^2(\mathbf{x}, z)]u(\mathbf{x}, z, \omega) = 0, \quad (6)$$

where ω denotes frequency, $V(\mathbf{x}, z)$ is velocity, and $u(\mathbf{x}, z, \omega)$ stands for the frequency-domain wavefield. For the 3D case, $\mathbf{x} = (x, y)$ and $\partial_x^2 = \partial_x^2 + \partial_y^2$.

The frequency-space-domain wavefield $u(\mathbf{x}, z, \omega)$ can be extrapolated in depth by any propagators P as follows:

$$u(\mathbf{x}, z + \Delta z, \omega) = P[u(\mathbf{x}, z, \omega)]. \quad (7)$$

Here the one-way LCB propagator is selected for its accuracy and efficiency (Wu et al., 2008). The wavefield is decomposed and propagated in the beamlet domain.

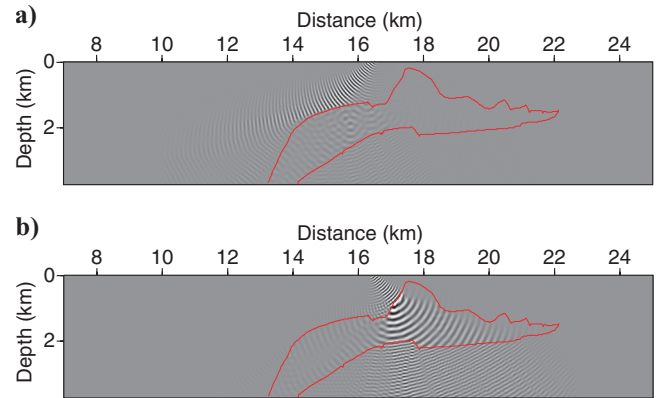


Figure 3. The LEF beamlet propagation in the SEG/EAGE salt model: (a) left-propagating LEF beamlet; (b) right-propagating LEF beamlet.

Wavefield decomposition using the LEF in the 2D case

At each depth z , the wavefield $u(x, z, \omega)$ can be decomposed into local exponential beamlets with windows along the horizontal x -axis:

$$\begin{aligned} u(x, z, \omega) &= \sum_n \sum_m \langle u(x, z, \omega), g_{mn}(x) \rangle g_{mn}(x) \\ &= \sum_n \sum_m [\hat{u}^{(+)}(\bar{x}_n, \bar{\xi}_m, z, \omega) g_{mn}^{(+)}(x) \\ &\quad + \hat{u}^{(-)}(\bar{x}_n, \bar{\xi}_m, z, \omega) g_{mn}^{(-)}(x)], \end{aligned} \quad (8)$$

where $\hat{u}^{(+)}(\bar{x}_n, \bar{\xi}_m, z, \omega)$ and $\hat{u}^{(-)}(\bar{x}_n, \bar{\xi}_m, z, \omega)$ are the coefficients for the corresponding right- and left-propagating LEF beamlets, respectively, located at the space window \bar{x}_n and local wavenumber window $\bar{\xi}_m$. The expression $\langle \cdot \rangle$ stands for the inner product as $\langle u(x, z, \omega), g_{mn}(x) \rangle = \int u(x, z, \omega) (g_{mn}(x))^* dx$ ($*$ denotes the complex conjugation).

If we use the LCB propagator, the LCB coefficients already are available during the wave propagation. After an extra LSB decomposition, the coefficients corresponding to local exponential beamlets can be calculated as follows:

$$\begin{cases} \hat{u}^{(+)}(\bar{x}_n, \bar{\xi}_m, z, \omega) = \frac{\hat{u}^{(c)}(\bar{x}_n, \bar{\xi}_m, z, \omega) - i\hat{u}^{(s)}(\bar{x}_n, \bar{\xi}_m, z, \omega)}{4} \\ \hat{u}^{(-)}(\bar{x}_n, \bar{\xi}_m, z, \omega) = \frac{\hat{u}^{(c)}(\bar{x}_n, \bar{\xi}_m, z, \omega) + i\hat{u}^{(s)}(\bar{x}_n, \bar{\xi}_m, z, \omega)}{4} \end{cases}, \quad (9)$$

where $\hat{u}^{(c)}(\bar{x}_n, \bar{\xi}_m, z, \omega)$ and $\hat{u}^{(s)}(\bar{x}_n, \bar{\xi}_m, z, \omega)$ are the complex coefficients of the LCB and LSB decomposition of the wavefield. The detailed derivation of the coefficient calculation is given in Appendix B.

The LEF decomposition translates the space-domain wavefield into the local space-wavenumber domain. For example, the total $2M$ coefficients $\hat{u}^{(+)}(\bar{x}_n, \bar{\xi}_m, z, \omega)$ and $\hat{u}^{(-)}(\bar{x}_n, \bar{\xi}_m, z, \omega)$ ($m = 0, \dots, M - 1$) represent the weights of the $2M$ directional beamlets in the localized window at position \bar{x}_n . The cartoon in Figure 4 shows the basic concept of the LEF beamlet decomposition. The LEF beamlet coefficients provide only the directional information for each window. However, we need the directional information for each point for the illumination analysis, which can be extracted from the beamlet coefficients by partial reconstruction. Through the partial reconstruction, the absolute directional information $u^{(+)}(x, z, \bar{\xi}_m, \omega)$ and $u^{(-)}(x, z, \bar{\xi}_m, \omega)$ (Appendix B) is obtained for each space point, which is a weighted average of two windowed plane waves of the same local wavenumber from the overlapped windows. It also can be thought of as an interpolation from the LEF decomposition coefficients. Collectively, $u^{(+)}(x, z, \bar{\xi}_m, \omega)$ and $u^{(-)}(x, z, \bar{\xi}_m, \omega)$ are local plane waves in the local wavenumber domain.

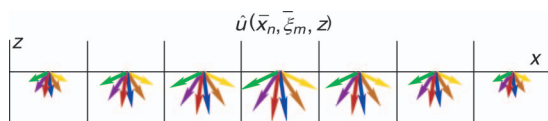


Figure 4. The concept of LEF beamlet decomposition.

Through a summation of the local plane waves with all of the local wavenumbers, the wavefield can be fully reconstructed:

$$u(x, z, \omega) = \sum_m [u^{(+)}(x, z, \bar{\xi}_m, \omega) + u^{(-)}(x, z, \bar{\xi}_m, \omega)]. \quad (10)$$

As we discussed earlier, the local wavenumber is related to the local propagating angle. For the local plane wave with the local wavenumber $\bar{\xi}_m$, the corresponding propagating angle is

$$\bar{\theta}_m = \arcsin\left(\frac{V(x, z)}{\omega} \bar{\xi}_m\right), \quad (11)$$

where $\bar{\theta}_m$ is the local propagating angle with respect to the vertical axis, and $V(x, z)$ is the velocity at (x, z) . With this relationship, we can get the directional information in the local angle domain. First we decompose the wavefield into the local wavenumber domain using the LEF and then interpolate the local wavenumber-domain wavefield to the local angle domain. As the transformation from the local wavenumber to the local angle is nonlinear, the angle resolution will be slightly different from the local slant-stacking method.

How can we choose the window length for the LEF decomposition? According to the Heisenberg uncertainty principle, the size of spatial and directional localization cannot be arbitrarily small. A larger window means higher angular resolution, but lower spatial resolution. Therefore, the window length should be chosen to balance the spatial and directional resolutions. Generally, the window length is related to the frequency, velocity, and grid size of the model. For example, the main frequency at 15 Hz is calculated with 3000 m/s as the maximum model velocity. Then the maximum wavelength is 200 m. If the grid size is 25 m, a wavelength covers eight grid points. Therefore, the window length for the LEF needs to cover a whole wavelength at least. In this case, we usually use 16 points as the window length, which provides sufficient directional information while maintaining appropriate spatial localization.

Wavefield decomposition using the LEF in the 3D case

In the 3D case, the 2D LEF atom is defined as follows:

$$\mathbf{g}_{mnpq}(\mathbf{x}) = \sqrt{\frac{2}{L_n L_q}} \mathbf{B}_{nq}(\mathbf{x}) \exp(i\bar{\xi}_{mp} \cdot (\mathbf{x} - \bar{\mathbf{x}}_{nq})), \quad (12)$$

where $\mathbf{x} = (x, y)$, $\bar{\mathbf{x}}_{nq} = (\bar{x}_n, \bar{y}_q)$, and $\bar{\xi}_{mp} = (\bar{\xi}_m, \bar{\eta}_p)$, with \bar{x}_n, \bar{y}_q as the window position in the x - and y -axes, and $\bar{\xi}_m, \bar{\eta}_p$ as the local wavenumber along the x - and y -directions. Due to the 2D nature of the elementary decomposition functions (frame vectors), the directivity can be divided into four quarters (see Appendix C for details). Appendix C gives the detailed definition of 2D LEF functions and the derivation of wavefield decomposition for 3D implementation.

In the 3D case, we also need the definition of local angles. For the local plane wave of the local horizontal wavenumber $\bar{\xi}_{mp} = (\bar{\xi}_m, \bar{\eta}_p)$, the corresponding propagating angle is

$$\bar{\theta}_{mp} = (\bar{\theta}_m, \bar{\varphi}_p) = (\arcsin(\sqrt{\bar{\xi}_m^2 + \bar{\eta}_p^2}/k), \arctan(\bar{\xi}_m/\bar{\eta}_p)). \quad (13)$$

The two components $\bar{\theta}_m$ and $\bar{\varphi}_p$ are the inclination angle with respect to the z -axis (zenith, downward in this case) and the azimuth angle with respect to the x -axis of the local plane wave, respectively

(shown in Figure 5). The expression $k = \omega / V(\mathbf{x}, z)$ represents the local wavenumber, and $V(\mathbf{x}, z)$ is the velocity at the subsurface point (\mathbf{x}, z) . The component $\bar{\theta}_m$ is from 0° to 90° , and the component $\bar{\varphi}_p$ is from -180° to 180° .

DIRECTIONAL ILLUMINATION ANALYSIS IN THE LOCAL ANGLE DOMAIN

For a given acquisition geometry (shown in Figure 6), we put a unit-strength source on the surface and propagate it to get the Green's function for each subsurface point. The frequency-space-domain Green's function from the source \mathbf{s} to a subsurface point (\mathbf{x}, z) can be decomposed into local angle components at the image region by the proposed LEF method, which is

$$G(\mathbf{x}, z; \mathbf{s}, \omega) = \sum_{\theta_s} G(\mathbf{x}, z, \theta_s; \mathbf{s}, \omega). \quad (14)$$

The expression $G(\mathbf{x}, z; \mathbf{s}, \omega)$ is the frequency-space Green's function, and $G(\mathbf{x}, z, \theta_s; \mathbf{s}, \omega)$ is its local angle component at θ_s . Similarly, the frequency-space Green's function from the subsurface point (\mathbf{x}, z) to a receiver \mathbf{g} can also be decomposed as follows:

$$G(\mathbf{x}, z; \mathbf{g}, \omega) = \sum_{\theta_g} G(\mathbf{x}, z, \theta_g; \mathbf{g}, \omega), \quad (15)$$

where $G(\mathbf{x}, z; \mathbf{g}, \omega)$ and $G(\mathbf{x}, z, \theta_g; \mathbf{g}, \omega)$ are the frequency-space Green's function and its local angle component at θ_g , respectively.

To evaluate the local angle-domain illumination for a given acquisition system, let us first define the directional illumination (DI) map. A DI map sums all contribution from the sources at the subsurface point. As the DI map is frequency dependent, a single-frequency DI map is calculated to illustrate the illumination energy distribution, such as the DI map for the dominant frequency ω_0 of the source. For the local propagating angle θ_s , the DI map for ω_0 is defined as

$$D_d(\mathbf{x}, z, \theta_s, \omega_0) = \sum_{\mathbf{s}} |G(\mathbf{x}, z, \theta_s; \mathbf{s}, \omega_0)|^2. \quad (16)$$

If we sum the illumination energy of all incident angles together, we can get the total illumination as follows:

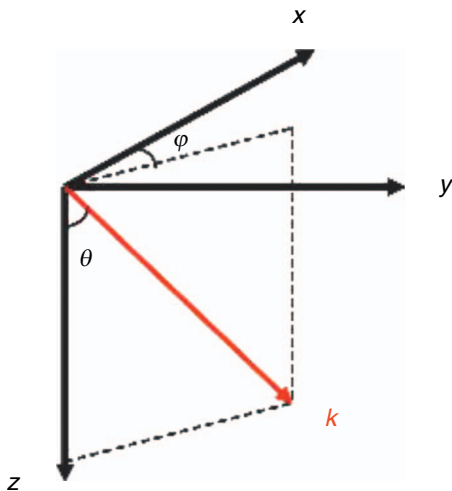


Figure 5. Definition of the incident angle $\theta = (\theta, \varphi)$ for the 3D case.

$$D_{\text{total}}(\mathbf{x}, z, \omega) = \sum_{\theta_s} \sum_{\mathbf{s}} |G(\mathbf{x}, z, \theta_s; \mathbf{s}, \omega)|^2. \quad (17)$$

A DI map shows only the angle distribution of illumination energy from the sources. To illustrate the aperture and propagation effects of the given acquisition geometry on energy distribution for a specific pair of incident/receiving angles, we use the unit impulse as the source at both source and receiver points and propagated to each space point. Similar to the procedure of DI mapping, we sum up the contribution of the Green's functions for each incident/receiving pair to get the acquisition aperture efficacy (AAE) matrix at each image point, which neglects the detailed wave-interference pattern and considers only the energy distribution in the space and angle domains for the acquisition configuration. Then the AAE matrix at point (\mathbf{x}, z) is defined as

$$E(\mathbf{x}, z, \theta_s, \theta_g, \omega) = \sum_{\mathbf{s}} |G(\mathbf{x}, z; \theta_s, \mathbf{s}, \omega)|^2 \sum_{\mathbf{g}} |G(\mathbf{x}, z; \theta_g, \mathbf{g}, \omega)|^2, \quad (18)$$

which measures the acquisition efficacy of a given acquisition system to any type of scattering objects.

However, when the objects are local reflectors (interfaces, faults, and so on), we can further reduce the AAE matrix at each point to a function of reflector dip by a summation of all of the reflected energy for a given dip,

$$A_d(\mathbf{x}, z, \theta_n, \omega) = \sum_{\theta_r} E(\mathbf{x}, z, \theta_n, \theta_r, \omega), \quad (19)$$

where $A_d(\mathbf{x}, z, \theta_n, \omega)$ is called the acquisition dip-response (ADR) vector for point (\mathbf{x}, z) ; θ_n is the reflector normal angle to the vertical (equal to the migration-dip angle); and θ_r is the reflection angle with respect to the normal, which can be obtained from θ_s and θ_g (Chen et al., 2006). The value of the ADR map measures the dip-angle response of the acquisition system, including the source and receiver apertures, and propagation effects. Figure 7 shows the difference between the DI and ADR maps.

NUMERICAL TESTS ON 2D AND 3D SEG/EAGE MODELS

Directional illumination analysis (DI and ADR maps) for the 2D SEG/EAGE model

We use both local slant-stacking and local exponential-beamlet methods for the directional illumination analysis of the 2D SEG/EAGE salt model, which has 1200 samples with an interval of 25 m in the horizontal direction and 150 samples with an interval of 25 m

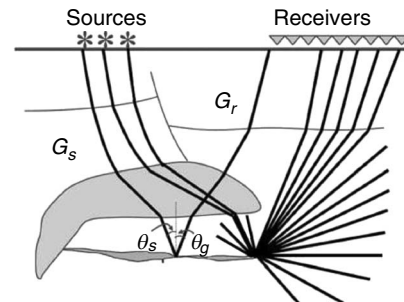


Figure 6. An illustration of acquisition geometry.

in depth. The minimum velocity is 1524 m/s, and the maximum velocity is 4480 m/s. There are 325 shots with an interval of 50 m, and each shot has 176 receivers in its left side with an interval of 25 m. From a comparison of the directional illumination maps (Figures 8 and 9), we see that the quality of analysis using the LEF method is similar to that of the more time-consuming local slant-stacking method. Some slight differences exist due to the lower redundancy and the procedure of interpolation from the local wavenumber domain to the local angle domain, which was discussed in the previous section.

Figure 10 shows the ADR maps from the new LEF method. With similar illumination results, the computational cost of the LEF method is only one-fourth that of the local slant-stacking method for this 2D example. These directional illumination results clearly explain the reason for the drastic variations in image amplitude and its dip dependency in the subsalt region. This efficient method can be developed further for fast acquisition aperture corrections, which will be discussed in future publications.

Let us briefly discuss the computational efficiency of the method in the 2D case. We compare this LEF method with the time-consuming local slant-stacking method and the Gabor-Daubechies (G-D) frame method. We assume the same window length L_{win} for the Gaussian window and the bell window, which correspond to the local slant-stacking (or G-D frame) and LEF beamlet decompositions, respectively. For the local slant-stacking method, a slant-stack computation with $O(L_{win} \times L_{win})$ is required for each sample point, which results in a total computational complexity of $O(N \times L_{win} \times L_{win})$ (N is the total sample number). For the G-D frame method, a fast Fourier transform (FFT) computation with $O(L_{win} \log_2 L_{win})$ is done for each Gaussian window. However, the G-D frame is not stable when the redundancy is two, which means we have to use more windows to evade this difficulty. If the redundancy is four, as we usually used, the G-D frame method needs a total computation of $O(4 \times N \times \log_2 L_{win})$.

On the other hand, for the LEF beamlet decomposition, we need only a local cosine transform (LCT) and a local sine transform (LST) computation with $O(L_{win} \log_2 L_{win}/4)$ (due to the use of the folding technique in the fast LCT and LST). Therefore, the LEF method needs a total computation of $O(2 \times N \times \log_2 L_{win}/4)$. For example, if $L_{win} = 16$, these three methods need $O(256 \times N)$, $O(16 \times N)$, and $O(4 \times N)$ computations, respectively. The other advantage of using the local exponential beamlets is the availability of LCB coefficients during the propagation, which saves some computational time for the LEF decomposition. In summary, the analysis using the LEF is much more efficient than using the local slant-stacking and G-D frame methods.

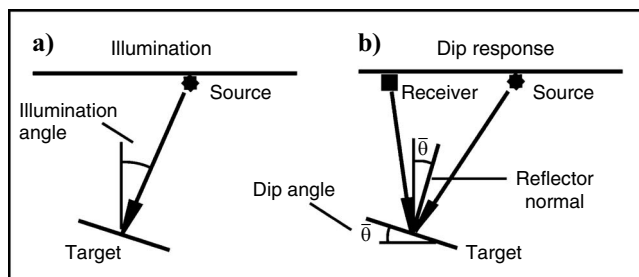


Figure 7. A sketch of the concept of DI and ADR.

Directional illumination analysis for different frequencies

We have mentioned that the directional illumination analysis is frequency dependent. To study the frequency-dependent effect, we first calculate and compare the directional illumination (DI) maps for a low frequency (5 Hz), the main frequency (15 Hz), and a high frequency (30 Hz). Figure 11 shows clearly that the angular resolution for the low frequency is much lower than that for the high frequency.

Figure 12 shows in detail the frequency-dependent effect of illumination variation. It plots the DI strength distribution for three frequencies along a horizontal line at a given depth ($z = 3.25$ km) for the incident angle of -30° . Within a narrow frequency band, the DI strength distribution is similar, but it changes significantly when the frequency difference is large. From this observation, we can develop some frequency-dependent illumination compensation methods for multifrequency bands to improve the image quality.

In our calculation, the same window length was used to do the beamlet decomposition for all frequencies. In this way, the window length (beamwidth) contains fewer wavelengths and therefore has a weaker focusing effect for low-frequency than for high-frequency waves. This means that for the same spatial resolution (space localization), the angular resolution is frequency dependent. The other option is to have a multiscale windowing scheme so that the angular resolution stays the same, but spatial resolution becomes frequency dependent.

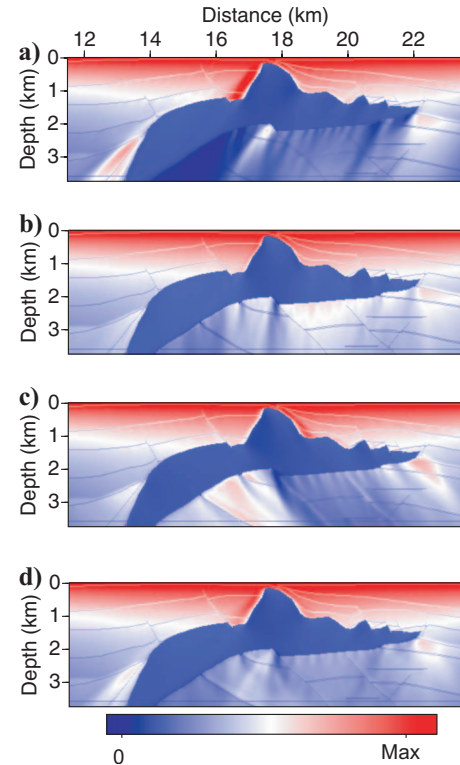


Figure 8. Directional illumination (DI) maps using the local slant-stacking method: (a) DI map for the incident angle $\theta_s = -30^\circ$; (b) DI map for the incident angle $\theta_s = 0^\circ$; (c) DI map for the incident angle $\theta_s = 30^\circ$; (d) total illumination.

Directional illumination analysis (DI maps and ADR maps) for the 3D SEG/EAGE model

In the 3D case, as we know, the computational growth is geometric. As a result, the local slant-stacking method and the G-D frame

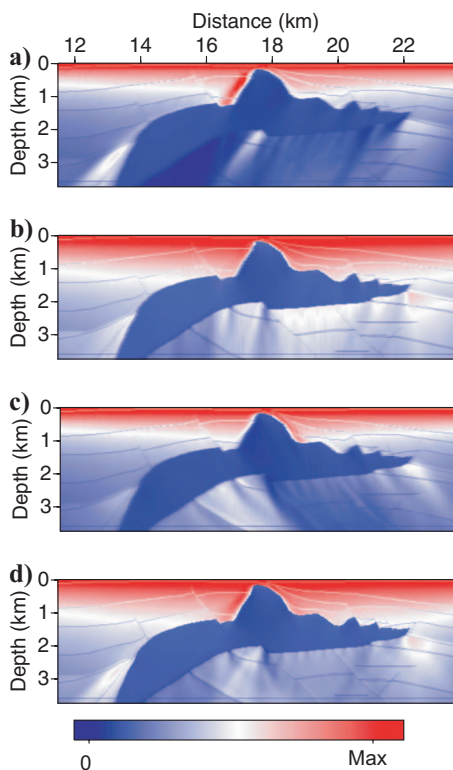


Figure 9. Directional illumination (DI) maps using the local exponential frame decomposition: (a) DI map for the incident angle $\theta_s = -30^\circ$; (b) DI map for the incident angle $\theta_s = 0^\circ$; (c) DI map for the incident angle $\theta_s = 30^\circ$; (d) total illumination.

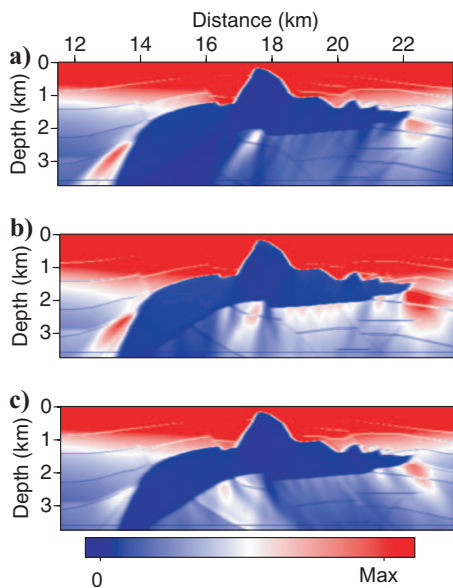


Figure 10. Acquisition dip response (ADR) using the local exponential frame decomposition: (a) ADR map for the dip angle $\theta_n = -20^\circ$; (b) ADR map for the dip angle $\theta_n = 0^\circ$; (c) ADR map for the dip angle $\theta_n = 20^\circ$.

method are quite time-consuming to use in 3D directional illumination. However, the LEF method is still affordable in the 3D case.

To demonstrate the application of the illumination analysis, we calculate numerical examples using the 3D SEG/EAGE salt velocity model. This example simulates the illumination condition of the 45-shot data set. The data set represents a land acquisition geometry. The grid size for the model consists of 676, 676, and 210 grids in the x -, y - and z -axes, respectively, with 20 m for the horizontal and depth intervals. The locations of those 45 shots are shown in Figure 13a. Each shot has 201×201 receivers with an interval of 20 m along both x - and y -directions. Figure 14 shows the vertical and horizontal slices (marked in Figure 13b) of the velocity model and migration image.

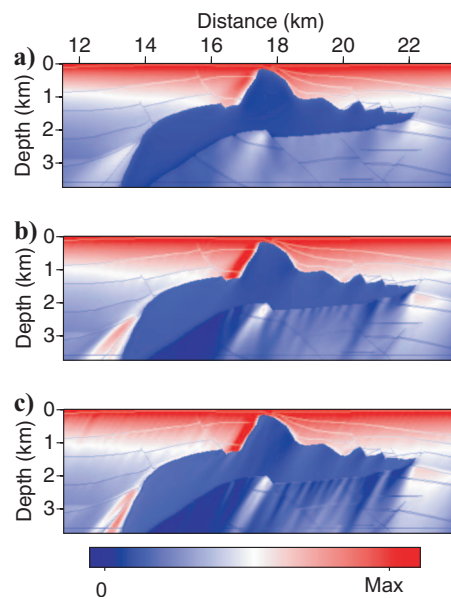


Figure 11. Directional illumination (DI) maps for the incident angle $\theta_s = -30^\circ$: (a) DI map for 5 Hz; (b) DI map for 15 Hz; (c) DI map for 30 Hz.

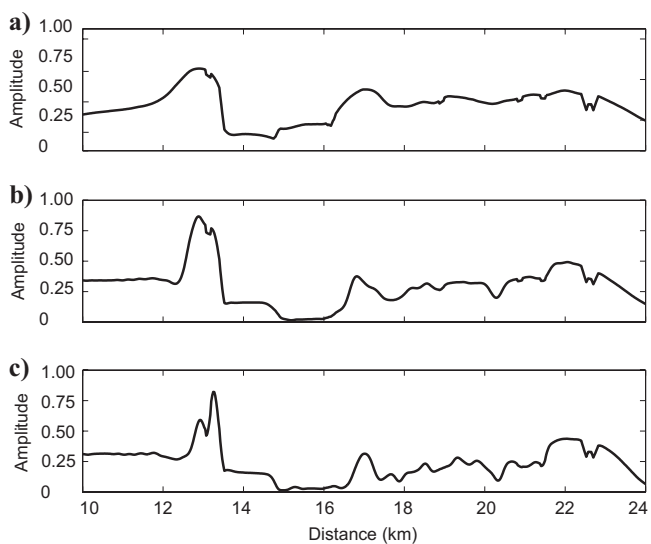


Figure 12. Directional illumination strength from low frequency to high frequency for the angle $\theta_s = -30^\circ$, at depth $n_z = 130$: (a) 5 Hz; (b) 15 Hz; (c) 30 Hz.

Figure 15 is the result of DI maps of different incident angles θ_s , including the y-left incidence ($\theta_s = 30^\circ, \varphi_s = -90^\circ$), vertical incidence ($\theta_s = 0^\circ, \forall \varphi_s$) and y-right incidence ($\theta_s = 30^\circ, \varphi_s = 90^\circ$), respectively. From the DI maps, we can clearly see the energy flux of different local angles, especially for the subsalt area. For the ADR calculation, a large amount of computation is needed to get each receiver's Green's function, and then we use some sampled receiver's Green's function to get the ADR maps. In this example, the sampling interval is eight for both x- and y-axes, which means we calculate one Green's function in every 8×8 grid.

Figure 16 shows the ADR maps calculated by the local exponential frame method. The dip-angle ranges are ($0^\circ < \theta_n < 90^\circ, \varphi_n = -90^\circ$), ($\theta_n = 0^\circ, \forall \varphi_n$), and ($0^\circ < \theta_n < 90^\circ, \varphi_n = 90^\circ$), which represent negative, zero, and positive dip responses, respectively. These figures show the different responses for different dip angles, which are due to the salt structure and the acquisition system. From Figure

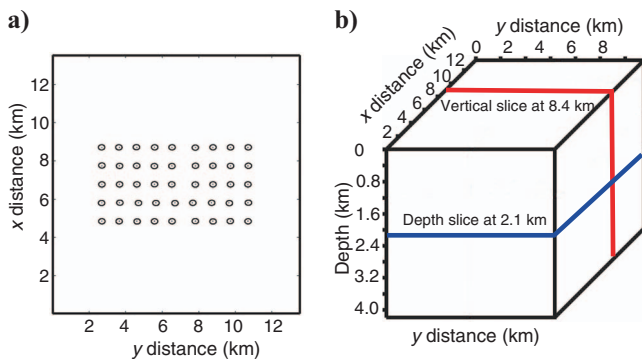


Figure 13. (a) Location of the 45 shots; (b) location of the slices for plotting.

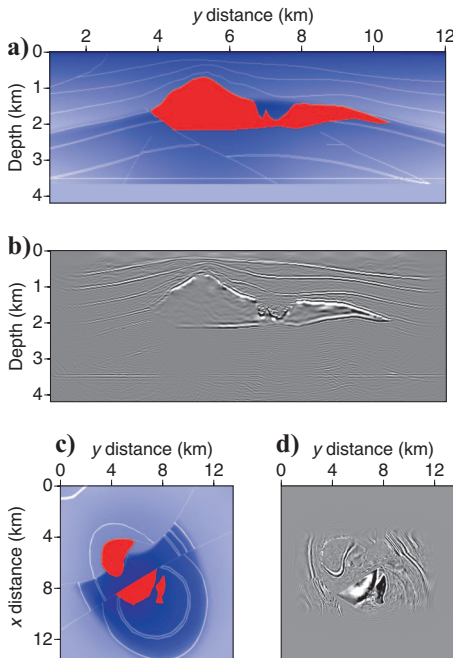


Figure 14. Velocity and image slices by LCB beamlet migration: (a) vertical slice of the velocity model; (b) vertical slice of the image; (c) horizontal slice of the velocity model; (d) horizontal slice of the image.

15, we see that the illumination with negative azimuthal angles is much poorer than that with positive azimuthal angles. Correspondingly, in Figure 16, the dip responses for reflectors with negative dips

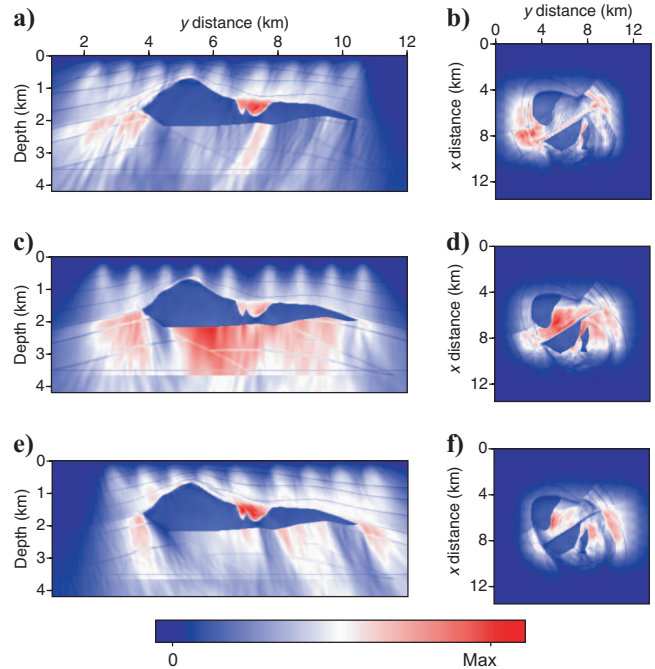


Figure 15. Directional illumination (DI) maps using the LEF: (a, b) DI for the angle ($\theta_s = 30^\circ, \varphi_s = -90^\circ$); (c, d) DI for the angle ($\theta_s = 0^\circ, \forall \varphi_s$); (e, f) DI for the angle ($\theta_s = 30^\circ, \varphi_s = 90^\circ$).

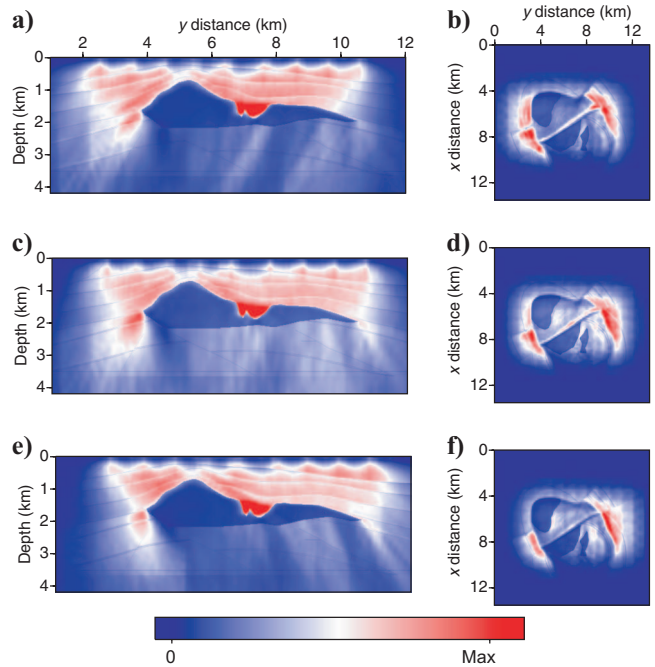


Figure 16. Acquisition dip-response (ADR) maps using the LEF: (a, b) ADR for the dip angle ($0^\circ < \theta_n < 90^\circ, \varphi_n = -90^\circ$); (c, d) ADR for the dip angle ($\theta_n = 0^\circ, \forall \varphi_n$); (e, f) ADR for the dip angle ($0^\circ < \theta_n < 90^\circ, \varphi_n = 90^\circ$).

are weaker than those with positive dips. From these directional illumination results, we can also explain the poor image quality of the subsalt area for reflectors with certain dip angles.

Let us also discuss the computational cost between the LEF method and the local slant-stacking method in the 3D case. According to the efficiency discussion in the 2D case, the basic computational cost is squared for these methods. If an $N \times N$ wavefield is decomposed, the local slant-stacking method needs an order of $O(N \times N \times L_{\text{win}} \times L_{\text{win}} \times L_{\text{win}} \times L_{\text{win}})$ computation, whereas the LEF method needs only $O(4 \times N \times N \times \log_2 L_{\text{win}}/4 \times \log_2 L_{\text{win}}/4)$ computation. In the case of $L_{\text{win}} = 16$, the computational costs for the LEF method and the local slant-stacking method are $O(16 \times N^2)$ and $O(65536 \times N^2)$, which means more than 4000 times the saving in CPU time for the wavefield decomposition.

In addition, the LEF method also reduces the memory and storage usage for the 3D case. In the illumination calculation, one Green's function can be used at different acquisition apertures of different shots. Therefore, the Green's functions are saved to avoid repetitive calculation. However, the local slant-stacking method will create $N \times N \times L_{\text{win}} \times L_{\text{win}}$ coefficients in the local angle domain, whereas the LEF method has only $4 \times N \times N$ coefficients. For a window length of $L_{\text{win}} = 16$, the memory saving will be 64 times greater. In a word, the local exponential frame provides a very efficient directional illumination method with a dramatic saving in internal memory usage.

CONCLUSIONS

We have developed an efficient method of directional illumination analysis in the local angle domain using local exponential-frame (LEF) beamlets, which form a tight frame of the redundancy ratio two. Due to the availability of the local cosine basis (LCB, an orthogonal decomposition) coefficients during wave propagation by using the LCB propagator, we need only an extra orthogonal decomposition (local sine transform) to get into the local angle domain. As the local cosine/sine transforms have fast algorithms, this method has a much higher efficiency than the Gabor-Daubechies frame method and the local slant-stacking method, especially in the 3D case. In the case of $L_{\text{win}} = 16$, where L_{win} is the window length of the LEF decomposition, the CPU saving over the local slant-stack method is more than 4000 times greater, and the memory saving is 64 times greater. Numerical examples of directional illumination maps and the acquisition dip responses for the 2D and 3D SEG/EAGE salt models illustrate the validity and efficiency of the new method. This method can be used to develop efficient algorithms for image amplitude compensation in the local angle domain for true-reflection imaging.

ACKNOWLEDGMENTS

We thank Xiaobi Xie, Jun Cao, Yingcai Zheng, Yaofeng He, Hui Yang, and Xiaofeng Jia for helpful discussions. The work is supported by the Wavelet Transform on Propagation and Imaging for Seismic Exploration (WTOPI) Project at the University of California, Santa Cruz.

APPENDIX A

THE BELL FUNCTION FOR LOCAL TRIGONOMETRIC BASES

The bell function can be defined as

$$B_n(x) = \begin{cases} 0, & x < \bar{x}_n - \varepsilon \\ \beta\left(\frac{x - \bar{x}_n}{\varepsilon}\right), & \bar{x}_n - \varepsilon \leq x < \bar{x}_n + \varepsilon \\ 1, & \bar{x}_n + \varepsilon \leq x \leq \bar{x}_{n+1} - \varepsilon' \\ \beta\left(\frac{\bar{x}_{n+1} - x}{\varepsilon'}\right), & \bar{x}_{n+1} - \varepsilon' < x \leq \bar{x}_{n+1} + \varepsilon' \\ 0, & x > \bar{x}_{n+1} + \varepsilon' \end{cases}. \quad (\text{A-1})$$

The expression $\beta(x)$ denotes a shape function (rising or decaying profile), which is defined as

$$\beta_{k+1}(x) = \beta_k\left(\sin \frac{\pi x}{2}\right) \quad \text{for } x \in [-1, 1], \quad (\text{A-2})$$

with $k \geq 0$, and

$$\beta_0(x) = \sin\left(\frac{4}{\pi}(1+x)\right) \quad \text{for } x \in [-1, 1]. \quad (\text{A-3})$$

The smoothness of $\beta_{k+1}(x)$ is associated with the parameter k . For example, for $k = 0$,

$$\beta_1(x) = \sin\left(\frac{4}{\pi}\left(1 + \sin \frac{\pi x}{2}\right)\right). \quad (\text{A-4})$$

Figure A-1 shows three bell functions with $k = 0$, $k = 2$, and $k = 4$.

The properties of the bell function,

$$\begin{cases} B_l(x)^2 + B_l(2\alpha - x)^2 = 1, & x \in [\alpha - \varepsilon, \alpha + \varepsilon] \\ B_l(x)^2 + B_l(2\beta - x)^2 = 1, & x \in [\beta - \varepsilon', \beta + \varepsilon'] \\ B_l(x) = 1, & x \in [\alpha + \varepsilon, \beta - \varepsilon'], \end{cases} \quad (\text{A-5})$$

ensure the orthonormality of the bases.

Bell functions can have all but an arbitrarily small amount of energy localized in just the positive part of the frequency. This is caused by the construction scheme of the localized bases and is related to the shape of the bell functions. The energy leakage is defined as the energy leaked to the negative frequency compared to the total energy. The energy leakage can be very small when k in equation A-2 is very large. However, a bell function with larger k has less frequency leakage, but has worse time-frequency localization because of the steep wall of the bell function. This is a compromise. In our calculation, we usually use a bell function with $k = 2$.

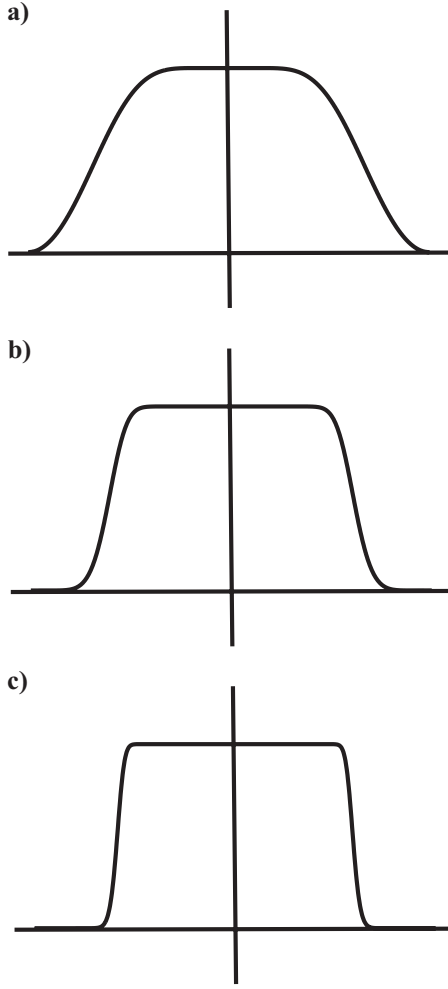


Figure A-1. Bell functions associated (from top to bottom) with (a) $k = 1$, (b) $k = 3$, and (c) $k = 5$.

APPENDIX B

DERIVATION OF WAVEFIELD DECOMPOSITION USING LOCAL EXPONENTIAL FRAMES

The frequency-space-domain wavefield $u(x, z, \omega)$ at depth z can be decomposed into beamlets along the x -axis with the local cosine basis (LCB) beamlet

$$u(x, z, \omega) = \sum_n \sum_m \hat{u}^{(c)}(\bar{x}_n, \bar{\xi}_m, z, \omega) b_{mn}^{(c)}(x) \quad (\text{B-1})$$

and the local sine basis (LSB) beamlet

$$u(x, z, \omega) = \sum_n \sum_m \hat{u}^{(s)}(\bar{x}_n, \bar{\xi}_m, z, \omega) b_{mn}^{(s)}(x), \quad (\text{B-2})$$

where $\hat{u}^{(c)}(\bar{x}_n, \bar{\xi}_m, z, \omega) = \langle u(x, z, \omega), b_{mn}^{(c)}(x) \rangle$ and $\hat{u}^{(s)}(\bar{x}_n, \bar{\xi}_m, z, \omega) = \langle u(x, z, \omega), b_{mn}^{(s)}(x) \rangle$ are decomposition coefficients of the LCB and the LSB, respectively. Both $\hat{u}^{(c)}(\bar{x}_n, \bar{\xi}_m, z, \omega)$ and $\hat{u}^{(s)}(\bar{x}_n, \bar{\xi}_m, z, \omega)$ are complex coefficients.

Then the wavefield can be described as a linear combination of the two above decompositions,

$$u(x, z, \omega) = \frac{1}{2} \sum_n \sum_m [\hat{u}^{(c)}(\bar{x}_n, \bar{\xi}_m, z, \omega) b_{mn}^{(c)}(x) + \hat{u}^{(s)}(\bar{x}_n, \bar{\xi}_m, z, \omega) b_{mn}^{(s)}(x)]. \quad (\text{B-3})$$

Substituting the local cosine and sine bases with their exponential expressions, we get

$$\begin{aligned} u(x, z) &= \frac{1}{2} \sum_n \sum_m \left\{ \hat{u}^{(c)}(\bar{x}_n, \bar{\xi}_m, z, \omega) \frac{1}{2} [g_{mn}^{(+)}(x) + g_{mn}^{(-)}(x)] \right. \\ &\quad \left. + \hat{u}^{(s)}(\bar{x}_n, \bar{\xi}_m, z, \omega) \frac{1}{2i} [g_{mn}^{(+)}(x) - g_{mn}^{(-)}(x)] \right\} \\ &= \sum_n \sum_m \left\{ \frac{\hat{u}^{(c)}(\bar{x}_n, \bar{\xi}_m, z, \omega) - i \hat{u}^{(s)}(\bar{x}_n, \bar{\xi}_m, z, \omega)}{4} g_{mn}^{(+)}(x) \right. \\ &\quad \left. + \frac{\hat{u}^{(c)}(\bar{x}_n, \bar{\xi}_m, z, \omega) + i \hat{u}^{(s)}(\bar{x}_n, \bar{\xi}_m, z, \omega)}{4} g_{mn}^{(-)}(x) \right\}. \end{aligned} \quad (\text{B-4})$$

As a result, the local exponential-decomposition coefficients can be calculated as

$$\begin{cases} \hat{u}^{(+)}(\bar{x}_n, \bar{\xi}_m, z, \omega) = \frac{\hat{u}^{(c)}(\bar{x}_n, \bar{\xi}_m, z, \omega) - i \hat{u}^{(s)}(\bar{x}_n, \bar{\xi}_m, z, \omega)}{4} \\ \hat{u}^{(-)}(\bar{x}_n, \bar{\xi}_m, z, \omega) = \frac{\hat{u}^{(c)}(\bar{x}_n, \bar{\xi}_m, z, \omega) + i \hat{u}^{(s)}(\bar{x}_n, \bar{\xi}_m, z, \omega)}{4} \end{cases}. \quad (\text{B-5})$$

Then the wavefield decomposition using the LEF can be expressed as

$$u(x, z, \omega) = \sum_n \sum_m \hat{u}^{(+)}(\bar{x}_n, \bar{\xi}_m, z, \omega) g_{mn}^{(+)}(x) + \hat{u}^{(-)}(\bar{x}_n, \bar{\xi}_m, z, \omega) g_{mn}^{(-)}(x). \quad (\text{B-6})$$

If we rewrite equation B-6 with the full expression of the LEF, we get

$$\begin{aligned} u(x, z, \omega) &= \sum_m \exp(i \bar{\xi}_m x) \sum_n \hat{u}^{(+)}(\bar{x}_n, \bar{\xi}_m, z, \omega) \sqrt{\frac{2}{L_n}} B_n(x) \\ &\quad \times \exp(-i \bar{\xi}_m \bar{x}_n) + \sum_m \exp(-i \bar{\xi}_m x) \sum_n \hat{u}^{(-)}(\bar{x}_n, \bar{\xi}_m, z, \omega) \\ &\quad \times \sqrt{\frac{2}{L_n}} B_n(x) \exp(i \bar{\xi}_m \bar{x}_n). \end{aligned} \quad (\text{B-7})$$

Therefore, the directional information for the space point (x, z) and local direction with $\bar{\xi}_m$ as the local wavenumber can be extracted by the partial reconstruction

$$\begin{cases} u^{(+)}(x,z,\bar{\xi}_m,\omega) = \exp(i\bar{\xi}_m x) \sum_n \hat{u}^{(+)}(\bar{x}_n, \bar{\xi}_m, z, \omega) \sqrt{\frac{2}{L_n}} B_n(x) \exp(-i\bar{\xi}_m \bar{x}_n) \\ u^{(-)}(x,z,\bar{\xi}_m,\omega) = \exp(-i\bar{\xi}_m x) \sum_n \hat{u}^{(-)}(\bar{x}_n, \bar{\xi}_m, z, \omega) \sqrt{\frac{2}{L_n}} B_n(x) \exp(i\bar{\xi}_m \bar{x}_n) \end{cases} \quad (\text{B-8})$$

Collectively, $u^{(+)}(x,z,\bar{\xi}_m,\omega)$ and $u^{(-)}(x,z,\bar{\xi}_m,\omega)$ are local plane waves in the local wavenumber domain.

APPENDIX C

LOCAL EXPONENTIAL FRAME EXTENSION FOR THE 3D CASE

2D local exponential frame

To use the LEF in the 3D case, we need expressions of the LEF for the 2D decomposition. The 2D LEF atoms can be defined as

$$\mathbf{g}_{mnpq}(\mathbf{x}) = \sqrt{\frac{2}{L_n L_q}} \mathbf{B}_{nq}(\mathbf{x}) \exp(i\bar{\xi}_{mp} \cdot (\mathbf{x} - \bar{\mathbf{x}}_{nq})), \quad (\text{C-1})$$

where $\mathbf{x} = (x,y)$, $\bar{\mathbf{x}}_{nq} = (\bar{x}_n, \bar{y}_q)$, and $\bar{\xi}_{mp} = (\bar{\xi}_m, \bar{\eta}_p)$. The expression \cdot stands for the dot product. The expressions $\mathbf{B}_{nq}(\mathbf{x}) = B_n(x)B_q(y)$ and $\mathbf{g}_{mnpq}(\mathbf{x})$ represent 2D functions.

The 2D LEF also can be written as follows:

$$\begin{cases} \mathbf{g}_{mnpq}^{(++)}(x,y) = \sqrt{\frac{4}{L_n L_q}} B_n(x) B_q(y) \exp(i\bar{\xi}_m(x - \bar{x}_n)) \exp(i\bar{\eta}_p(y - \bar{y}_q)) \\ \mathbf{g}_{mnpq}^{(+-)}(x,y) = \sqrt{\frac{4}{L_n L_q}} B_n(x) B_q(y) \exp(i\bar{\xi}_m(x - \bar{x}_n)) \exp(-i\bar{\eta}_p(y - \bar{y}_q)) \\ \mathbf{g}_{mnpq}^{(-+)}(x,y) = \sqrt{\frac{4}{L_n L_q}} B_n(x) B_q(y) \exp(-i\bar{\xi}_m(x - \bar{x}_n)) \exp(i\bar{\eta}_p(y - \bar{y}_q)) \\ \mathbf{g}_{mnpq}^{(--)}(x,y) = \sqrt{\frac{4}{L_n L_q}} B_n(x) B_q(y) \exp(-i\bar{\xi}_m(x - \bar{x}_n)) \exp(-i\bar{\eta}_p(y - \bar{y}_q)) \end{cases} \quad (\text{C-2})$$

where the superscripts $(++)$, $(+-)$, $(-+)$, and $(--)$ denote the different azimuthal directions in the 3D case. The 2D LEF is also a tight frame with the redundancy of 4, which can also be implemented by linear combinations of the 2D local trigonometric basis (LTB).

The relationship between the 2D LEF and 2D LTB is

$$\begin{cases} \mathbf{g}_{mnpq}^{(++)}(\mathbf{x}) = (\mathbf{b}_{mnpq}^{(cc)}(\mathbf{x}) + i\mathbf{b}_{mnpq}^{(cs)}(\mathbf{x})) + i(\mathbf{b}_{mnpq}^{(sc)}(\mathbf{x}) + i\mathbf{b}_{mnpq}^{(ss)}(\mathbf{x})) \\ \mathbf{g}_{mnpq}^{(+-)}(\mathbf{x}) = (\mathbf{b}_{mnpq}^{(cc)}(\mathbf{x}) - i\mathbf{b}_{mnpq}^{(cs)}(\mathbf{x})) + i(\mathbf{b}_{mnpq}^{(sc)}(\mathbf{x}) - i\mathbf{b}_{mnpq}^{(ss)}(\mathbf{x})) \\ \mathbf{g}_{mnpq}^{(-+)}(\mathbf{x}) = (\mathbf{b}_{mnpq}^{(cc)}(\mathbf{x}) + i\mathbf{b}_{mnpq}^{(cs)}(\mathbf{x})) - i(\mathbf{b}_{mnpq}^{(sc)}(\mathbf{x}) + i\mathbf{b}_{mnpq}^{(ss)}(\mathbf{x})) \\ \mathbf{g}_{mnpq}^{(--)}(\mathbf{x}) = (\mathbf{b}_{mnpq}^{(cc)}(\mathbf{x}) - i\mathbf{b}_{mnpq}^{(cs)}(\mathbf{x})) - i(\mathbf{b}_{mnpq}^{(sc)}(\mathbf{x}) - i\mathbf{b}_{mnpq}^{(ss)}(\mathbf{x})) \end{cases} \quad (\text{C-3})$$

where $\mathbf{b}_{mnpq}^{(cc)}(\mathbf{x})$, $\mathbf{b}_{mnpq}^{(cs)}(\mathbf{x})$, $\mathbf{b}_{mnpq}^{(sc)}(\mathbf{x})$, and $\mathbf{b}_{mnpq}^{(ss)}(\mathbf{x})$ are 2D LTB functions. Take $\mathbf{b}_{mnpq}^{(cs)}(\mathbf{x})$ as an example:

$$\mathbf{b}_{mnpq}^{(cs)}(\mathbf{x}) = b_{mn}^{(c)}(x) b_{pq}^{(s)}(y). \quad (\text{C-4})$$

Wavefield decomposition using the LEF in the 3D case

The 2D wavefield in the x - y plane can be decomposed by the 2D local exponential frames

$$\begin{aligned} u(\mathbf{x}, z, \omega) &= \sum_n \sum_m \sum_q \sum_p \langle u(\mathbf{x}, z, \omega), \mathbf{g}_{mnpq}(\mathbf{x}) \rangle \mathbf{g}_{mnpq}(\mathbf{x}) \\ &= \sum_n \sum_m \sum_q \sum_p [\hat{u}^{(++)}(\bar{\mathbf{x}}_{nq}, \bar{\xi}_{mp}, z, \omega) \mathbf{g}_{mnpq}^{(++)}(\mathbf{x}) \\ &\quad + \hat{u}^{(+-)}(\bar{\mathbf{x}}_{nq}, \bar{\xi}_{mp}, z, \omega) \mathbf{g}_{mnpq}^{(+-)}(\mathbf{x}) + \hat{u}^{(-+)} \\ &\quad \times (\bar{\mathbf{x}}_{nq}, \bar{\xi}_{mp}, z, \omega) \mathbf{g}_{mnpq}^{(-+)}(\mathbf{x}) + \hat{u}^{(--)} \\ &\quad \times (\bar{\mathbf{x}}_{nq}, \bar{\xi}_{mp}, z, \omega) \mathbf{g}_{mnpq}^{(--)}(\mathbf{x})]. \end{aligned} \quad (\text{C-5})$$

Let $\hat{u}_{mnpq}^{(++)}(z)$, $\hat{u}_{mnpq}^{(+-)}(z)$, $\hat{u}_{mnpq}^{(-+)}(z)$, and $\hat{u}_{mnpq}^{(--)}(z)$ represent $\hat{u}^{(++)} \times (\bar{\mathbf{x}}_{nq}, \bar{\xi}_{mp}, z, \omega)$, $\hat{u}^{(+-)} \times (\bar{\mathbf{x}}_{nq}, \bar{\xi}_{mp}, z, \omega)$, $\hat{u}^{(-+)} \times (\bar{\mathbf{x}}_{nq}, \bar{\xi}_{mp}, z, \omega)$, and $\hat{u}^{(--)} \times (\bar{\mathbf{x}}_{nq}, \bar{\xi}_{mp}, z, \omega)$; then the LEF decomposition coefficients can be calculated as follows:

$$\begin{cases} \hat{u}_{mnpq}^{(++)}(z) = \frac{1}{16} (\hat{u}_{mnpq}^{(cc)}(z) - i\hat{u}_{mnpq}^{(cs)}(z) - i\hat{u}_{mnpq}^{(sc)}(z) - \hat{u}_{mnpq}^{(ss)}(z)) \\ \hat{u}_{mnpq}^{(+-)}(z) = \frac{1}{16} (\hat{u}_{mnpq}^{(cc)}(z) + i\hat{u}_{mnpq}^{(cs)}(z) - i\hat{u}_{mnpq}^{(sc)}(z) + \hat{u}_{mnpq}^{(ss)}(z)) \\ \hat{u}_{mnpq}^{(-+)}(z) = \frac{1}{16} (\hat{u}_{mnpq}^{(cc)}(z) - i\hat{u}_{mnpq}^{(cs)}(z) + i\hat{u}_{mnpq}^{(sc)}(z) + \hat{u}_{mnpq}^{(ss)}(z)) \\ \hat{u}_{mnpq}^{(--)}(z) = \frac{1}{16} (\hat{u}_{mnpq}^{(cc)}(z) + i\hat{u}_{mnpq}^{(cs)}(z) + i\hat{u}_{mnpq}^{(sc)}(z) - \hat{u}_{mnpq}^{(ss)}(z)) \end{cases} \quad (\text{C-6})$$

where $\hat{u}_{mnpq}^{(cc)}(z)$, $\hat{u}_{mnpq}^{(cs)}(z)$, $\hat{u}_{mnpq}^{(sc)}(z)$, and $\hat{u}_{mnpq}^{(ss)}(z)$ are the complex coefficients of the LTB decomposition of the wavefield. The derivation is similar to that in the 2D case.

The partial reconstruction expression of the wavefield is

$$\begin{aligned} u(\mathbf{x}, \bar{\xi}_{mp}, \omega) &= \exp(i\bar{\xi}_{mp} \cdot \mathbf{x}) \sum_n \sum_q \hat{u}_z(\bar{\mathbf{x}}_{nq}, \bar{\xi}_{mp}, \omega) \\ &\quad \times \sqrt{\frac{4}{L_n L_q}} \mathbf{B}_{nq}(\mathbf{x}) \exp(-i\bar{\xi}_{mp} \cdot \bar{\mathbf{x}}_{nq}), \end{aligned} \quad (\text{C-7})$$

which represents a directional local plane wave in the 3D case.

REFERENCES

- Alai, R., and J. Thorbecke, 2008, Illumination of the subsurface towards identifying shadow zones and optimizing target images: 78th Annual International Meeting, SEG, Expanded Abstracts, 193–197.
- Audebert, F., L. Nicoletis, and P. Froidevaux, 2005, Regularization of illumination in angle domains — A key to true amplitude migration: The Leading Edge, **24**, 643–654.
- Auscher, P., 1994, Remarks on the local Fourier bases, in J. J. Benedetto and M. W. Frazier, eds., Wavelets, mathematics, and applications: CRC Press, 203–218.
- Balian, R., 1981, Un principe d'incertitude en théorie du signal ou en mécanique quantique: Comptes Rendus de l'Académie des Sciences Série 2, 292, 1357–1362.
- Bear, G., C. Liu, R. Lu, D. Willen, and I. Watson, 2000, The construction of subsurface illumination and amplitude maps via ray tracing: The Leading Edge, **19**, 726–728.

- Berkhout, A. J., 1997, Pushing the limits of seismic imaging: Part 1 — Prestack migration in terms of double dynamic focusing: *Geophysics*, **62**, 937–954.
- Cao, J., and R. S. Wu, 2005, Influence of propagator and acquisition aperture on image amplitude: 75th Annual International Meeting, SEG, Expanded Abstracts, 1946–1949.
- , 2008, Amplitude compensation for one-way wave propagators in inhomogeneous media and its application to seismic imaging: *Communications in Computational Physics*, **3**, 203–221.
- , 2009, Full-wave directional illumination analysis in the frequency domain: *Geophysics*, **74**, 85–93.
- Chen, L., R. S. Wu, and Y. Chen, 2006, Target-oriented beamlet migration based on Gabor-Daubechies frame decomposition: *Geophysics*, **71**, no. 2, S37–S52.
- Claerbout, J. F., 1985, *Imaging the earth's interior*: Blackwell Scientific Publications.
- Coifman, R. R., and Y. Meyer, 1991, Remarques sur l'analyse de Fourier à fenêtre: *Comptes Rendus de l'Académie des Sciences Série I*, 312, 259–261.
- Daubechies, I., 1992, *Ten lectures on wavelets*: Society for Industrial and Applied Mathematics.
- Daubechies, I., S. Jaffard, and J.-L. Journé, 1991, A simple Wilson orthonormal basis with exponential decay: *SIAM Journal on Mathematical Analysis*, **22**, 554–573.
- Droujinine, A., B. Salomons, D. van Daalen, and F. Kuiper, 2008, WAZ wavefield de-remigration illumination analysis and sub-salt model building: 78th Annual International Meeting, SEG, Expanded Abstracts, 3697–3700.
- Eigen, J. T., 2008, Wave equation illumination using sparse-frequency one-way wavefield extrapolation: 78th Annual International Meeting, SEG, Expanded Abstracts, 2132–2136.
- Fontecha, B., W. Cai, F. Ortigosa, Q. Liao, S. Jin, and S. Xu, 2005, Wave equation migration and illumination on a 3-D GOM deep water data set: 75th Annual International Meeting, SEG, Expanded Abstracts, 1989–1992.
- Gjøystdal, H., E. Iversen, I. Lecomte, T. Kaschwich, Å. Drottning, and J. Mispel, 2007, Improved applicability of ray tracing in seismic acquisition, imaging, and interpretation: *Geophysics*, **72**, 261–271.
- Hoffmann, J., 2001, Illumination, resolution, and image quality of PP- and PS-waves for survey planning: *The Leading Edge*, **20**, 1008–1014.
- Lecomte, I., 2008, Resolution and illumination analyses in PSDM: A ray-based approach: *The Leading Edge*, **27**, 650–663.
- Le Rousseau, J. H., and M. V. de Hoop, 2001, Scalar generalized-screen algorithms in transversely isotropic media with a vertical symmetry axis: *Geophysics*, **66**, 1538–1550.
- Luo, M. Q., J. Cao, X. B. Xie, and R. S. Wu, 2004, Comparison of illumination analysis using one-way and full-wave propagators: 74th Annual International Meeting, SEG, Expanded Abstracts, 67–70.
- Mallat, S., 1999, *A wavelet tour of signal processing*, second edition: Academic Press.
- Muerdter, D., M. Kelly, and D. Ratcliff, 2001, Understanding subsalt illumination through ray-trace modeling: Part 2 — Dipping salt bodies, salt peaks, and nonreciprocity of subsalt amplitude response: *The Leading Edge*, **20**, 688–687.
- Muerdter, D., and D. Ratcliff, 2001a, Understanding subsalt illumination through ray-trace modeling: Part 1 — Simple 2D salt models: *The Leading Edge*, **20**, 578–594.
- , 2001b, Understanding subsalt illumination through ray-trace modeling: Part 3 — Salt ridges and furrows, and impact of acquisition orientation: *The Leading Edge*, **20**, 803–816.
- Rickett, J. E., 2003, Illumination-based normalization for wave-equation depth migration: *Geophysics*, **68**, 1371–1379.
- Ristow, D., and T. Rühl, 1994, Fourier finite-difference migration: *Geophysics*, **59**, 1882–1893.
- Schneider, W. A., and G. A. Winbow, 1999, Efficient and accurate modeling of 3-D seismic illumination: 69th Annual International Meeting, SEG, Expanded Abstracts, 633–636.
- Wang, Y. Z., R. Cook, and R. S. Wu, 2003, 3D local cosine beamlet propagator: 73rd Annual International Meeting, SEG, Expanded Abstracts, 981–984.
- Wang, Y. Z., and R. S. Wu, 2002, Beamlet prestack depth migration using local cosine basis propagator: 72nd Annual International Meeting, SEG, Expanded Abstracts, 1340–1343.
- Wickerhauser, M. V., 1994, Adapted wavelet analysis from theory to software: A. K. Peters.
- Wu, R. S., and L. Chen, 2002, Mapping directional illumination and acquisition aperture efficacy by beamlet propagators: 72nd Annual International Meeting, SEG, Expanded Abstracts, 1352–1355.
- , 2003, Prestack depth migration in angle-domain using beamlet decomposition: Local image matrix and local AVA: 73rd Annual International Meeting, SEG, Expanded Abstracts, 973–976.
- , 2006, Directional illumination analysis using beamlet decomposition and propagation: *Geophysics*, **71**, no. 4, S147–S159.
- Wu, R. S., L. Chen, and X. B. Xie, 2003, Directional illumination and acquisition dip-response: 65th Conference and Exhibition, EAGE, Extended Abstracts, P147.
- Wu, R. S., M. Luo, S. Chen, and X.-B. Xie, 2004, Acquisition aperture correction in angle-domain and true-amplitude imaging for wave equation migration: 74th Annual International Meeting, SEG, Expanded Abstracts, 937–940.
- Wu, R. S., and J. Mao, 2007, Beamlet migration using local harmonic bases: 77th Annual International Meeting, SEG, Expanded Abstracts, 2230–2234.
- Wu, R. S., Y. Wang, and J. H. Gao, 2000, Beamlet migration based on local perturbation theory: 70th Annual International Meeting, SEG, Expanded Abstracts, 1008–1011.
- Wu, R. S., Y. Wang, and M. Q. Luo, 2008, Beamlet migration using local cosine basis: *Geophysics*, **73**, 207–217.
- Xie, X. B., S. W. Jin, and R. S. Wu, 2003, Three-dimensional illumination analysis using wave-equation based propagator: 73rd Annual International Meeting, SEG, Expanded Abstracts, 989–992.
- , 2006, Wave-equation-based seismic illumination analysis, *Geophysics*, **71**, no. 5, S169–S177.
- Xie, X. B., and R. S. Wu, 1998, Improve the wide angle accuracy of screen method under large contrast: 68th Annual International Meeting, SEG, Expanded Abstracts, 1811–1814.
- , 2002, Extracting angle domain information from migrated wavefield: 72nd Annual International Meeting, SEG, Expanded Abstracts, 1360–1363.
- Xie, X. B., and H. Yang, 2008, A full-wave equation based seismic illumination analysis method: 70th Conference and Exhibition, EAGE, Extended Abstracts, P284.
- Yu, J., B. Hornby, and G. T. Schuster, 2005, Enhancing illumination of 3D VSP data by migration deconvolution: 75th Annual International Meeting, SEG, Expanded Abstracts, 380–383.